How brittle detachments form and evolve through space and time

C. Zuccari [a,f,*], F. Mazzarini [b], E. Tavarnelli [c], G. Viola [a], L. Aldega [d], V. Moretto [d], R. Xie [e], G. Musumeci [f]

[a] Department of Biological, Geological and Environmental Sciences, University of Bologna, Bologna, Italy
[b] Istituto Nazionale di Geofisica e Vulcanologia, Seismology & Tectonophysics Department, Roma, Italy
[c] Department of Physics, Earth and Environmental Sciences, University of Siena, Siena, Italy
[d] Department of Earth Sciences, Sapienza University of Rome, Rome, Italy
[e] Geological Survey of Norway, Trondheim, Norway
[f] Department of Earth Sciences, University of Pisa, Pisa, Italy

ABSTRACT

We report the first absolute deformation ages for the Mykonos Detachment that juxtaposes, in the context of the current Aegean rifting, Miocene siliciclastic deposits in the hanging wall against metabasites and synkinematic granites in the footwall. We identified and characterised 16 brittle structural facies (BSFs) within the detachment fault architecture through fieldwork, optical microscopy, and X-ray diffraction. BSFs dating by K-Ar of synkinematic mixed layer illite-smectite shows that the preserved BSFs formed during repeated slip events, thus constraining protracted faulting between 13.5 and 6.5 Ma. Dating, structural and mineralogical characterisation allowed for the time-constrained evaluation of the activation/de-activation of the involved deformation mechanisms and of the processes, including (i) fault zone nucleation, (ii) deformation partitioning, (iii) cataclasis, gouge formation and (iv) the final deformation localisation, that govern the evolution of brittle detachments, shaping the local current upper crustal structure. Our results provide new insights into the understanding of wide active and fossil rift systems.

1. Introduction

Temporal constraints on protracted and complex geological histories are necessary to understand the characteristics and intricacies of the governing geodynamic and tectonic processes (e.g., Fossen and Cavalcante, 2017; Tartaglia et al., 2020). Extensional detachments (brittle and ductile) represent remarkable players of such histories, thus deserving to be analysed in detail (e.g., Lister and Davis, 1989; Lee and Lister, 1992; Singleton et al., 2014; Heineke et al., 2019). Unfortunately, long-lasting and continuously localising strain and deformation therein tend to obliterate much of the evidence of their progressive evolution in space and time, which, at the outcrop, is represented by complex shear zone and fault architectures accommodating superposed multiple deformation events (e.g., Braathen et al., 2009; Musumeci et al., 2015; Tartaglia et al., 2020). These records may be found in highly localised structural domains, whose identification, characterisation and dating thus becomes crucial.

Even though extensional detachments have been thoroughly investigated as key features in areas of significant crustal extension and in the exhumation of deeply subducted and buried rocks (e.g., Ring et al., 1999; Mehl et al., 2005; Mancktelow et al., 2016; Rossetti et al., 2017; Coleman et al., 2019; Jolivet et al., 2021; Montemagni and Zanchetta, 2022), only little attention has so far been paid to the time-constrained reconstruction of their progressive development following initial localisation. Additionally, most studies focused on extensional detachments wherein brittle deformation and related structures form only by reactivating and exploiting inherited and ductile structures (e.g., thick mylonitic shear zones) during the late stages of the detachment evolution *en route* to surface (e.g., Lister and Davis, 1989; Lee and Lister, 1992; Dinter and Royden, 1993; Gautier et al., 1993; Grosjean et al., 2004; Mehl et al., 2005, 2007; Johnston et al., 2007; Vignaroli et al., 2009; Jolivet et al., 2010; Lecomte et al., 2010; Rossetti et al., 2017; Wu et al., 2020). In those systems, most of the extension and the overall detachment history have been temporally constrained by essentially dating the ductile fabrics (e.g., Hartz et al., 2000; Isik et al., 2004; Mulch et al., 2005; Cottle et al., 2007; Schneider et al., 2013; La Roche et al., 2016), whereas only little attention has so far been paid to the brittle structures. This mostly reflects the challenges of dating brittle deformation,

---

* Corresponding author.
  E-mail address: costantino.zuccari2@unibo.it (C. Zuccari).

particularly in the case of architecturally complex mature faults (e.g., Van Der Pluijm et al., 2001; Haines and van der Pluijm, 2012; Torgersen and Viola, 2014; Aldega et al., 2019; Viola et al., 2022; Tartaglia et al., 2023). However, conceptual and analytical advances with the K-Ar dating of synkinematic illite and mixed layer illite-smectite formed during multiple faulting episodes within the same fault now allow for the deconvolution of even complex fault histories deriving from repeated fault activation over long time spans (e.g., Viola et al., 2016).
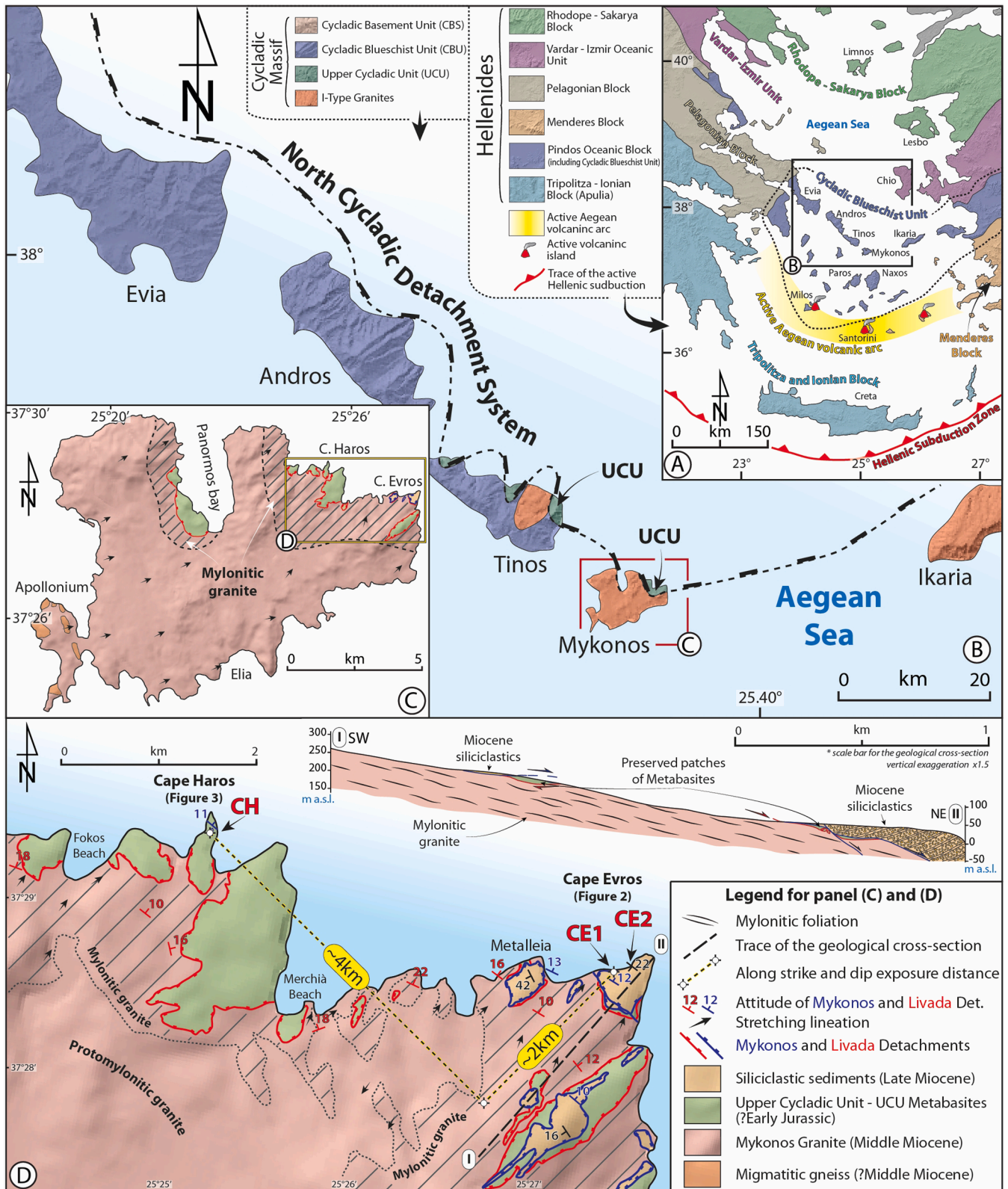

Fig. 1. Tectonic map of the Aegean region (A) and western Cyclades (B). (C) General setting of Mykonos Island. (D) Schematic geological setting of the northeastern Mykonos Island. Modified after Gazzola et al. (2023).

To understand the time-constrained progressive localisation and architectural development of the brittle component of extensional detachments, we present a detailed analysis of the brittle Mykonos Detachment (MD–Aegean Sea, Greece), which represents a regional scale detachment that nucleated and evolved entirely under brittle conditions, without exploiting former ductile fabrics (e.g., Lecomte et al., 2010). We propose an evolutionary model for the MD that only a high-resolution analysis of its internal architecture and the dating of many fault domains made possible. By coupling structural analysis, X-ray diffraction and K-Ar dating of seven gouge samples, we have constrained continuous deformation over at least ~7 Myrs (from ~14 Ma to ~6.5 Ma), i.e., from the first fault structuring phase to the last extreme deformation localisation recorded by the fault. We show that brittle deformation was highly compartmentalised, and migrated progressively dip-ward along the detachment during increasing displacement, in response to the formation, cooling and progressive exhumation of a synkinematic pluton in the footwall of the detachment. Based on an unprecedented structural/geochronological resolution, we thus provide quantitative insights into the modes of brittle detachment formation and evolution in space and time, which may assist in the interpretation of similar tectonic features elsewhere.

2. Geological setting

Mykonos Island in the central Aegean Sea (Fig. 1A-B) geologically pertains to the Hellenides, which are composed of a stack of continental (Pelagonian and Apulia) and oceanic (Pindos and Vardar) units (Fig. 1A). The evolution of this portion of the Hellenides can be related to the contractional formation of the Cycladic Massif (Fig. 1B), climaxing in the Cretaceous-Oligocene, during the convergence between Africa and European plates (e.g., Rosenbaum et al., 2002; Jolivet and Brun, 2010; Aravadinou et al., 2022; Gazzola et al., 2023). Clearcut evidence of this contractional phase, however, are not preserved on Mykonos Island, whose tectonic evolution and present-day structural configuration are instead mainly related to a phase of post-orogenic collapse (e.g., Jolivet and Faccenna, 2000; Jolivet et al., 2010). This collapse, climaxing in Miocene time and related to the slab roll-back-driven Aegean rifting (e.g., Hejl et al., 2002; Jolivet et al., 2015), steered the exhumation of the HP-LT rocks of the blueschist Cycladic complex (not exposed in Mykonos Island), favoured by the activation of multiple regional scale north- and south-dipping extensional detachments (e.g., the North Cycladic Detachment System - NCDS and the South Cycladic Detachment System; e.g., Jolivet and Faccenna, 2000; Brichau et al., 2006, 2010; Jolivet et al., 2010; Jolivet and Brun, 2010; Ring et al., 2011; Grasemann et al., 2012; Mancktelow et al., 2016, 2018; Bakowsky et al., 2023; Fig. 1).

Mykonos Island is mainly composed of a ~13–15 Ma old granite (Fig. 1C-D), intruded during crustal extension within the Cycladic basement (micaschist, migmatitic gneiss and marble) that is exposed only in the westernmost part of the Island (Apollonia peninsula; Fig. 1C) and in the nearby islands of Delos and Rhenia (e.g., Faure et al., 1991; Jolivet et al., 2010; Lecomte et al., 2010). The syntectonic granite, which compositionally varies between monzogranitic to leucogranitic (e.g., Lecomte et al., 2010; Gazzola et al., 2023), mainly crops out in central and eastern Mykonos and is structurally overlain by a suite of Jurassic metabasites, which were intruded by the granite starting in the Middle Miocene (Fig. 1C; e.g., Brichau et al., 2008; Bolhar et al., 2010). The preserved tectonostratigraphic sequence on Mykonos Island is topped by Miocene syntectonic siliciclastic deposits that tectonically rest on the metabasites or the granite (e.g., Sànchez-Goméz et al., 2002; Lecomte et al., 2010). However, a well-constrained age is not yet available for those sedimentary deposits, their inferred age being only based on dated clasts from the upper portion of the siliciclastic succession (Sànchez-Goméz et al., 2002).

The northeastern sector of the island is dissected by the ductile Livada Detachment (juxtaposing the metabasites against the granite; Figs. 1C-D and S1) and the brittle Mykonos Detachment (bringing the Miocene siliciclastic deposits onto the metabasites/granite; Fig. 1C and D), both belonging to the North Cycladic Detachment System (Fig. 1B; Jolivet et al., 2010; Glodny and Ring, 2022; Gazzola et al., 2023). Extension began under ductile conditions at ~15–14 Ma (age of granite crystallisation; e.g., Bolhar et al., 2010). The granite intruded the- and it is in tectonic contact with both the Cycladic basement and the metabasites of the Upper Cycladic Unit (Fig. 1). The tectonic contact is represented by the thick and laterally continuous mylonitic shear zone of the basal Livada Detachment (LD; e.g., Jolivet et al., 2010; Lecomte et al., 2010; Menant et al., 2013). The LD, which presumably accommodated a significant component of the bulk tectonic displacement on Mykonos Island, and promoted the exhumation and cooling of the granite in the footwall, is spectacularly exposed in the central-northern portion of the Island (Fokos and Mersini localities; Figs. 1, and S1A-C) and towards Cape Evros in the north-east (Fig. S1D and E). Mylonitic to ultra-mylonitic fabrics there overprint the granite and commonly also the metabasites (Fig. S1), with a clear top-to-the NE sense of the tectonic transport, locally also transposing aplitic dikes and sills related to the emplacement of the Miocene granite (Fig. S1A-C; e.g., Menant et al., 2013).

Brittle deformation associated with the MD is instead believed to have localised starting ~10 Ma ago (e.g., Jolivet et al., 2010, 2021), it being only partially coeval with ductile strain localisation along the LD (e.g., Lecomte et al., 2010).

3. Methods

Our structural analysis followed the Brittle Structural Facies (BSF) approach by Tartaglia et al. (2020), whereby a BSF comprises a rock volume formed by a specific fault rock type, mineral assemblage, colour, texture, and age. Some of the BSFs defined in our study (Figs. 2, 3, 4 and 5) are composed of gouges that we sampled for K-Ar dating on synkinematic mixed layer illite-smectite. Where visible, cross-cutting relationships between juxtaposed BSFs were used to constrain their relative timing of formation. Different gouge generations and BSFs were recognised by: (i) a different colour with respect to the surrounding BSFs (e.g., BSF4, Fig. 5A), (ii) sharp structural boundaries delimiting the identified gouges (e.g., BSF6, Fig. 5C), (iii) a specific composition as appreciable in the field (i.e., granular vs. plastic or cohesive vs. un-cohesive) and (iv) a specific structural style (e.g., BSFH3 which corresponds to a C-surface within a SC/C' domain). Every gouge (and thus the related BSF) was then dated by K-Ar so as to constrain the time dimension of the detachment evolution. The numbering of BSFs is based on their structural and geometrical position at the outcrops, thus adopting a sequential numbering from the base to the top of the fault zone (e.g., BSF1 and BSF7 thus being the lowermost and uppermost recognised BSFs at the CE1 exposure, respectively). Samples were collected by carefully avoiding potential mixing between different gouges (i.e., different BSFs), in order to constrain possible multiple activations of the fault, as recorded by each gouge. About 2 kg of material were sampled for each gouge.

K-Ar geochronology of syn-kinematic clay minerals from seven gouge samples was performed to constrain the timing of fault activation at the Cape Evros and Cape Haros exposures (see below). Separation of grain size fractions and K-Ar dating were performed at the Geological Survey of Norway (NGU), Trondheim, by following the standard analytical procedure for the separation, characterisation and dating of fault gouges used at the NGU Lab. More in detail, five grain-size fractions (from 6-10 to <0.1 μm) were separated, characterised and dated from gouges following the procedure by Viola et al. (2018). Illite polytype determinations by Rietveld refinement were performed to assess the proportion of detrital illite/muscovite ($2M_1$ polytype) vs. synkinematic illite-smectite ($1M_d$ polytype) formed during faulting. Polytype proportions were normalised to 100 % (Table 1; Fig. S5) and plotted as apparent K-Ar date vs. % of detrital illite/muscovite, and linearly
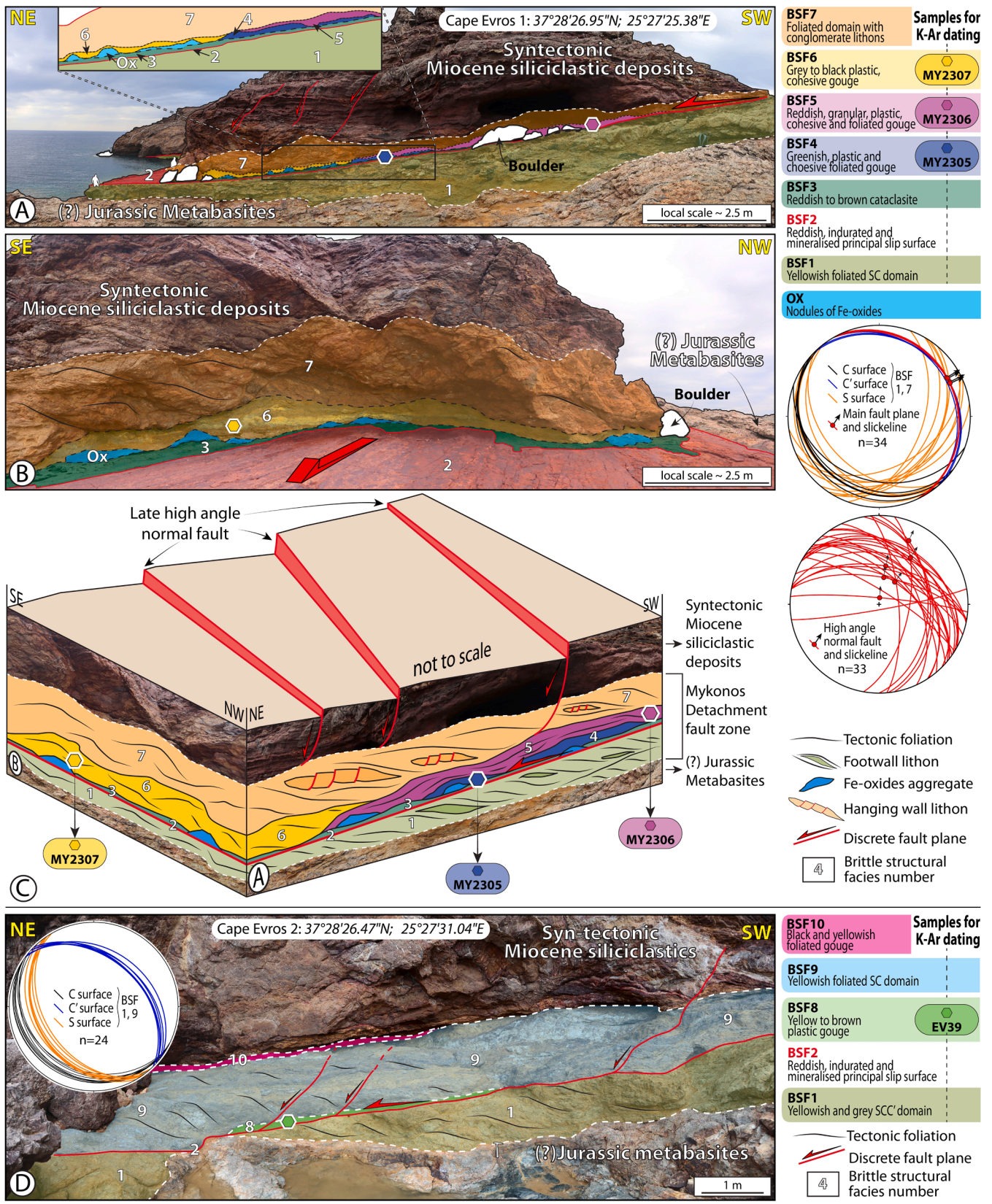
Fig. 2. Along-dip (A) and along strike (B) view of the Mykonos Detachment in the Cape Evros 1 section. (C) Schematic diagram (not to scale) portraying the three-dimensional architecture of the detachment and the mutual cross-cutting relationships among different BSFs. Stereographic projections refer to structures in A-B-C. (D) Along-dip view of the Mykonos Detachment in the Cape Evros 2 section with stereographic projections referring to structures in panel (D). Gouges collected for K-Ar dating are shown.
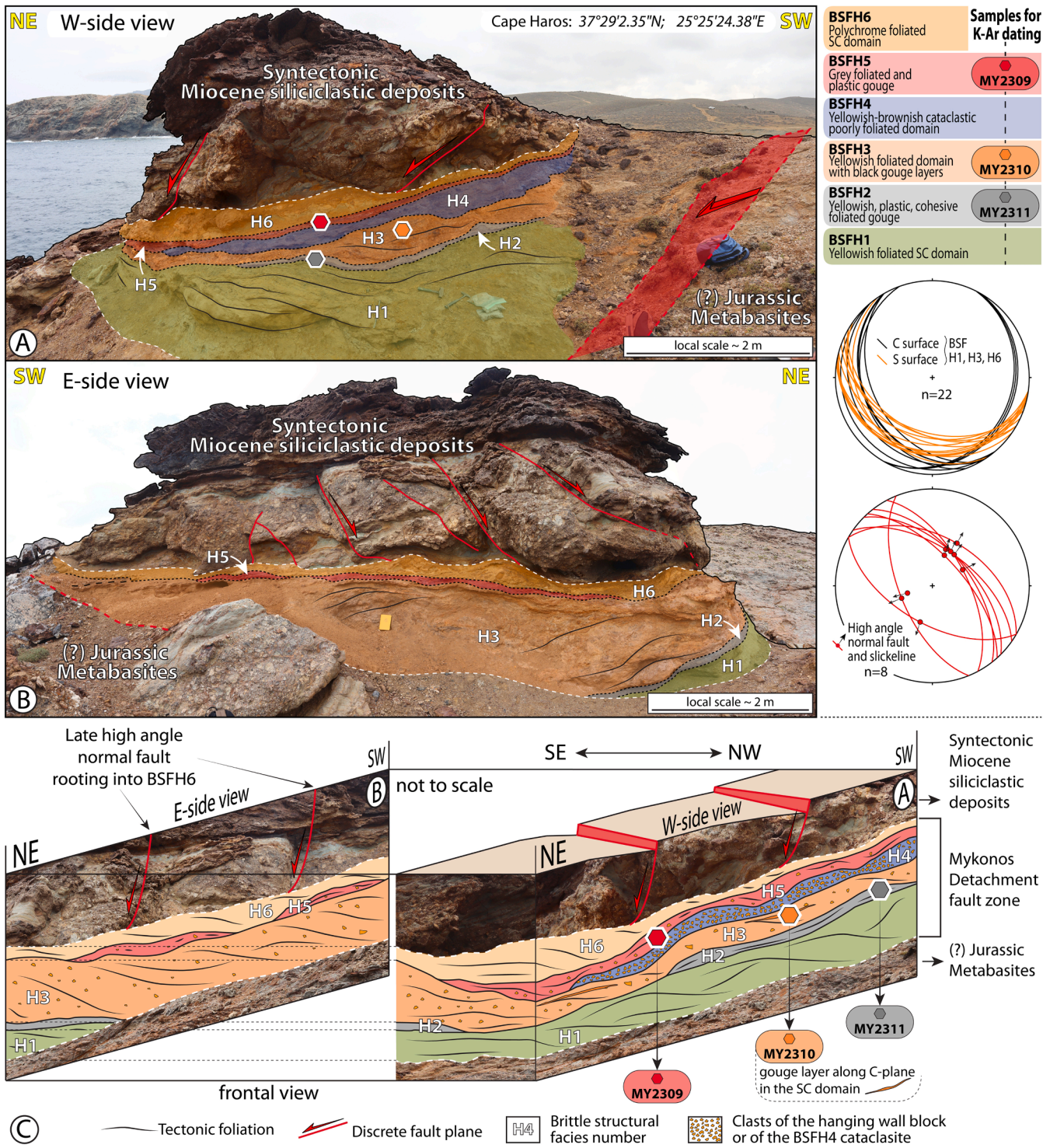
Fig. 3. Western (A) and eastern side (B) view of the Mykonos Detachment in Cape Haros with location of the recognised BSFs. (C) Schematic diagram (not to scale) portraying the three-dimensional architecture of the detachment and the mutual cross-cutting relationships among different BSFs. The dotted lines indicate the lateral continuation of the BSFs. Stereographic projections refer to structures in A-B-C. Gouges collected for K-Ar dating are shown.

extrapolated to 0 % and 100 % illite/muscovite-$2M_1$ by York regression. The last slip event age corresponds to the intercept on the Y-axis (Illite Age Analysis, IAA; Pevear, 1999; Curzi et al., 2024).

4. Results

The MD was studied at three outcrops (Figs. 2, 3, S2 and S3). Outcrops Cape Evros 1 and 2 (CE1-CE2, respectively; Fig. 2), in northeastern

Mykonos Island, are located along the detachment ~2 km down-dip from the Cape Haros (CH) site (Fig. 1D). At all outcrops, the MD is a spectacular top-to-the-NE fault zone juxtaposing Miocene siliciclastic deposits in the hanging wall (Figs. 1, 2 and 3) against the metabasites (Upper Cycladic Unit; Fig. 1) in the footwall (Figs. 2 and 3).

Outcrop CE1 is located on the western side of Cape Evros (*37°28′26.34″N; 25°27′24.38″E*; Fig. 2A), whereas CE2 is located toward the tip of the promontory (*37°28′26.55″N; 25°27′30.38″E*; Fig. 2D). CH
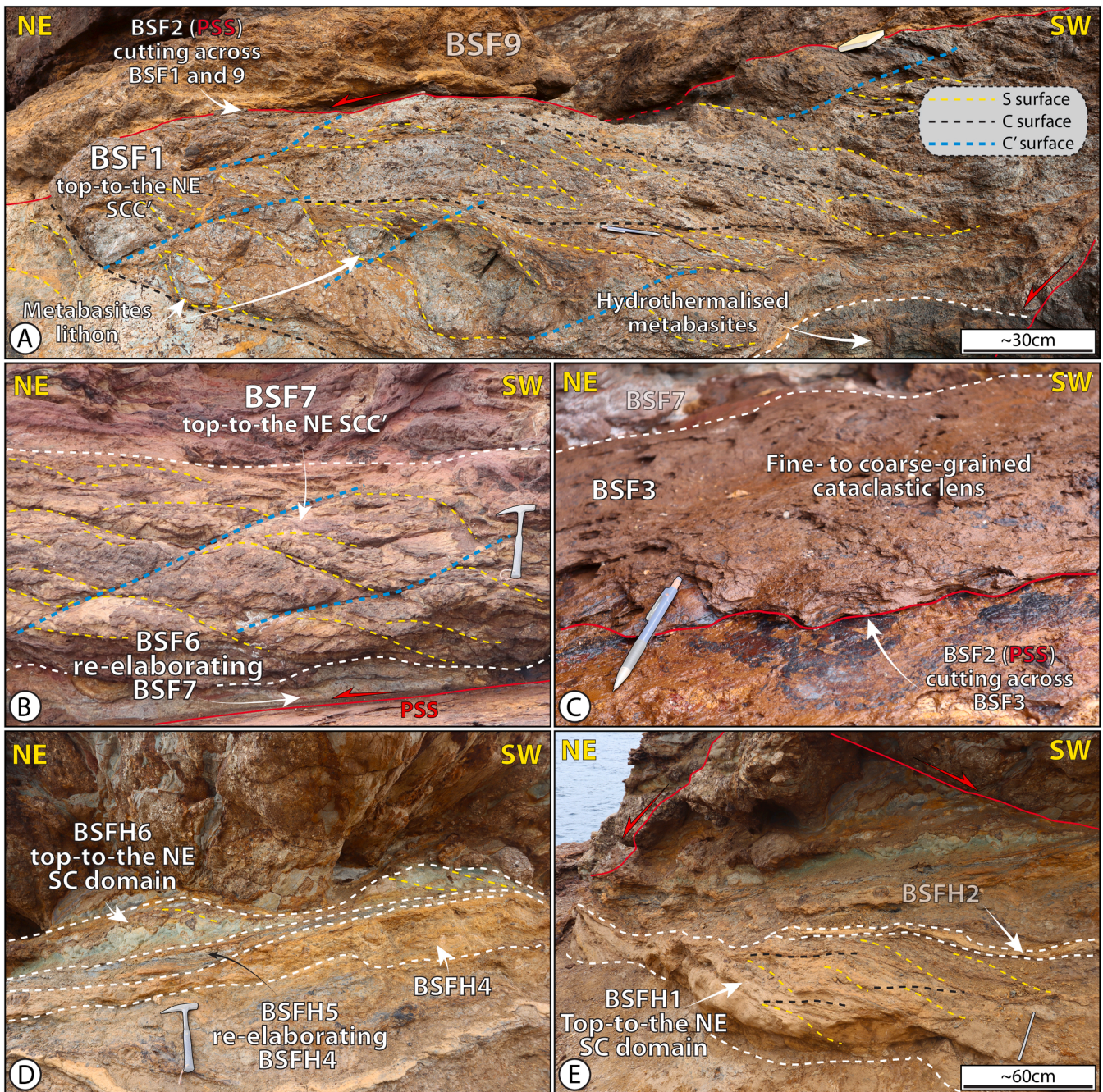
Fig. 4. Examples of Brittle Structural Facies at the Cape Evros and Cape Haros outcrops. (A) Top-to-the NE SC/C' domain of BSF1 cut at the top by the principal slip surface of BSF2 at outcrop CE2. (B) Top-to-the NE SC/C' domain of BSF7 re-elaborated by the plastic grey and blackish gouge of BSF6 that cuts the S surfaces of the SC/C' domain (outcrop CE1). (C) BSF3 rReddish cataclasite cut at the base by the principal slip surface of BSF2 at outcrop CE1. (D) Overview of the top-to-the NE SC domain of BSFH6 at CH, and of the gouge of BSFH5 that cuts and re-elaborates the cataclasite of BSFH4. (E) Overview of the basal top-to-the NE SC domain of outcrop CH truncated at the top by BSFH2.

instead crops out in a more internal part of Mykonos Island (*37°28′26.09′′N; 025°27′31.45′′E*; Figs. 1 and 3), to the northwest of Cape Evros. The fault zone is from ~1 to ~5 m thick and at all outcrops is sandwiched between SC/C' foliated domains, formed at the expense of both the footwall and the hanging wall, exhibiting a general top-to-the NE sense of shear (Figs. 2 and 3). In both the upper and lower foliated domains, variably sized slivers and lithons of metabasite (in the footwall) and conglomerate (in the hanging wall) are embedded within the SC/C' foliation. The MD fault core is characterised by several layers of cataclasites and plastic gouges, which show mutually cross-cutting relationships. In order to architecturally define all the structures above,

the identification and characterisation of the various BSFs are described below.

4.1. Brittle structural facies analysis

At CE1, the MD forms a ~3–4 m thick fault zone sandwiched by two SC/C' domains (Figs. 2A-C and S2A-B), which correspond to BSF1 and 7, respectively, that are composed of metabasites in the footwall and of Miocene siliciclastic deposits in the hanging wall (Figs. 2 and 4A-B). Decimetre- to metre-scale slivers and lithons of both metabasites and siliciclastics deposits are locally dismembered and transposed within
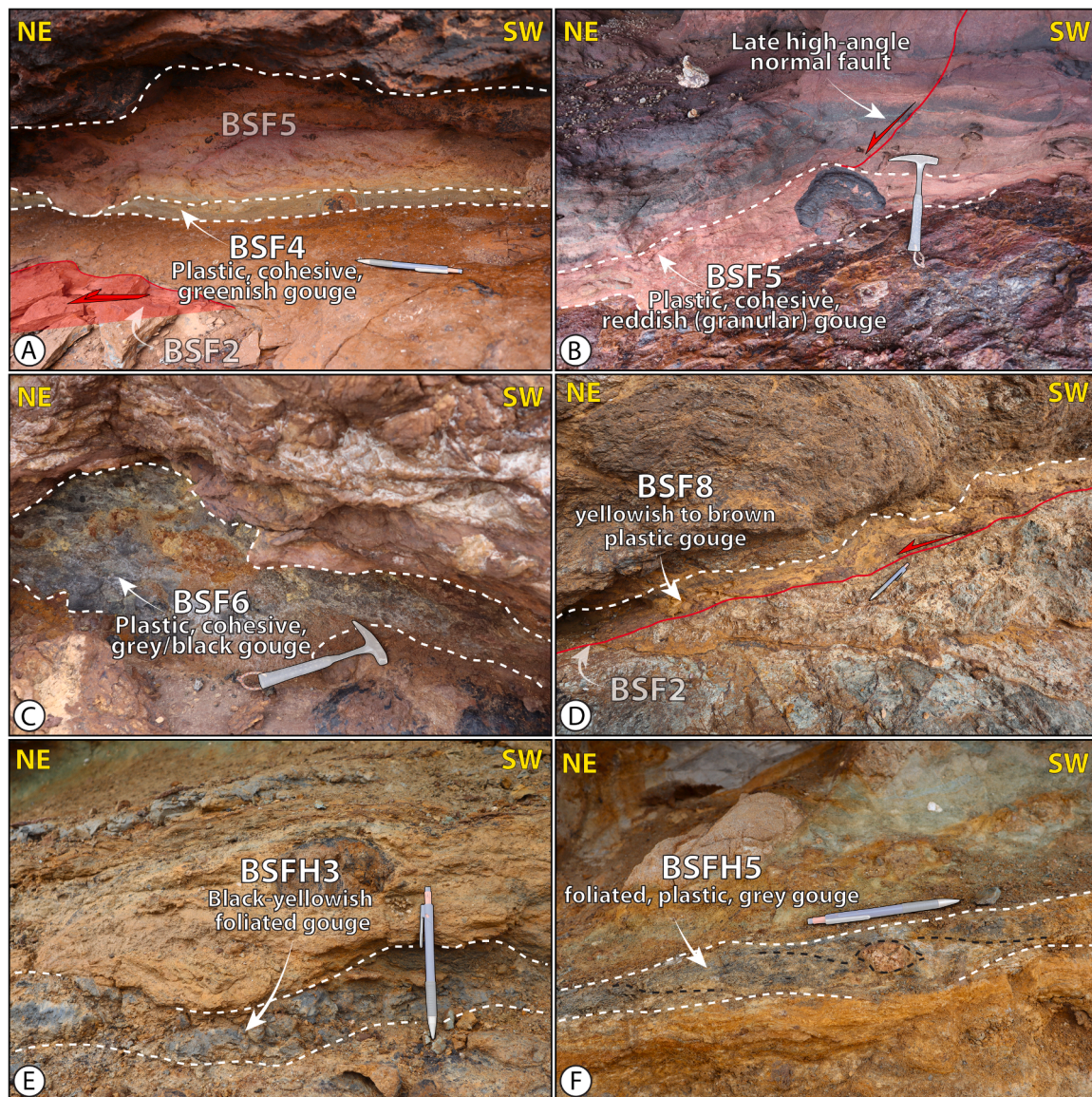
Fig. 5. Details of gouges sampled for K-Ar dating. (A) Plastic cohesive and greenish gouge lensoidal layer of BSF4 from outcrop CE1. Note the cross-cutting relationships between BSFs 4 and 5. (B) Sampled plastic, cohesive reddish granular gouge layer of BSF5 from outcrop CE1. Note the FeO-rich nodules cutting the foliation of BSF5. (C) Plastic, cohesive and grey/black gouge of BSF6 from outcrop CE1. (D) Yellowish to brown plastic gouge of BSF8 from outcrop CE2. Note that the PSS of BSF2 sharply cuts BSF8 at the base. (E) Black and yellowish gouge layer of BSFH3 along C plane from outcrop CH. (F) Structurally higher foliated and plastic grey gouge of BSFH5 from CH.

BSF1 and 7. The laterally continuous coarse- to fine-grained reddish cataclasite forming BSF3, mainly formed at the expense of the hanging wall siliciclastic deposits, cuts across-, reworks and partially deforms BSF1 and 7 (Figs. 2A-C and 4C) and is in turn cut and reworked by the foliated greenish gouge of BSF4 (Figs. 2A-C and 5A), which is formed by laterally discontinuous lenses of plastic material with a few dispersed clasts of the hanging wall block. The BFS4 foliation is in turn cut by the laterally continuous, granular and ~0.4 m thick foliated reddish gouge of BSF5 (Figs. 2A-C and 5B), which reaches its maximum thickness in the southwestern part of outcrop CE1 (Fig. 2C), and geometrically cuts downwards across the gouge of the BSF4. The clastic content of BSF5 is mainly composed of hanging wall block reworked material. The gouge-rich core of the fault is topped by the thick and lensoidal plastic black/grey gouge of BSF6, which composes the northeastern core of exposure CE1 and is well exposed in the along-strike section of the outcrop (Fig. 2B-C and 5C), without clear evidence of cross-cutting relationships to the other gouges. However, also in this case BSF6 partially reworks

the SC/C' domains of BSF1 and 7. All BSFs, however, are dissected by BSF2, which is made of a sharp, reddish strongly Fe-oxides mineralised (e.g., Menant et al., 2013) principal slip surface (Figs. 2A-C and 4A-C), attesting to late slip localisation. Multiple late high-angle normal faults accommodating centimetric displacements also dissect the detachment core as well as the SC/C' domains, eventually rooting into the PSS or exploiting gouge-rich layers to propagate (such as BSF5, Fig. 5B). These faults represent the youngest structures within the detachment architecture.

At CE2 (Fig. 2D), the MD is made of a ~3 m thick fault zone floored by the ~50 cm thick SC/C' domain of BSF1 (Fig. 4A), formed at the expense of the footwall metabasites, which are commonly dismembered and transposed into centimetre- to decimetre-thick lithons within- the SC/C' fabrics. The structurally higher SC/C' BSF9 (Fig. 2D) formed, in contrast, at the expense of the siliciclastic deposits of the hanging wall and forms a significant part of the fault zone. The yellow and laterally continuous foliated and cohesive BSF8 gouge (Figs. 2D and 5D) is

embedded between- and partially deforms the two MD bounding SC/C' domains, with clasts mainly from the siliciclastic deposits. The top of the exposed fault zone is marked by the black, lensoidal and foliated BSF10 gouge (Fig. 2D), which is transitional to the hanging wall. As in the case of CE1, the youngest recognised structure is a sharp slip surface (BSF2; Figs. 2D and 5D) that cuts across all other BSFs and on which, as in the case of CE1, root multiple high-angle normal faults that dissect all the other BSFs.

The MD in Cape Haros is composed of a ~3 m thick fault zone, generally yellow in colour, displaying strong deformation partitioning within the whole fault zone volume. The fault zone is bounded by two SC/C' domains (BSFH1 and H6; Figs. 3A-C and 4D-E), formed at the expense of the metabasites at the bottom and the Miocene siliciclastic deposits at the top, respectively, and locally reworking lithons and blocks of the hanging wall and footwall blocks. C planes within the fault zone are at times decorated by the variably thick (from 2 to > 10 cm) gouge layers of BSFH2 and small C planes within BSFH3 (Figs. 3 and 5E). Both of these BSFs contain yellowish to brown foliated gouge stringers. The SC/C' domains are interrupted by the continuous and ~20 cm thick yellowish and poorly consolidated cataclasite of BSFH4 (Figs. 3C and 4D), composed of clasts of metabasites and siliciclastic deposits dispersed within a clay-rich matrix. BSFH4 is cut and deformed by the thin black and poorly foliated gouge of BSFH5, which embeds the earlier cataclasite clasts (Fig. 3C and 5F) and remains below the upper SC/C' domain, which is, in turn, overlain by the siliciclastic deposits (Fig. 3).

4.2. Gouge compositional data

Thirty-five grain size fractions (6–10, 2–6, 0.4–2, 0.1–0.4, and <0.1 µm) were analysed to evaluate the distribution of synkinematic and detrital minerals within the gouge samples (Table 1, Figs. 5 and 6). All samples generally show the same bulk composition, which varies with respect to the grain-size fraction (Table 1, Fig. 6). Four samples were collected from outcrops Cape Evros 1 (MY2305 – BSF4, MY2306 – BSF5, MY2307 – BSF6) and Cape Evros 2 (EV39 – BSF8) and three further samples from Cape Haros (MY2309 – BSFH5, MY2310 – BSFH3, and MY2311 – BSFH2). All samples are a mixture of detrital and synkinematic clay minerals (long-range ordered mixed layers illite-smectite with $1M_d$ polytypysm). In the coarser fractions of all samples (6–10, 2–6 µm), inherited minerals such as quartz, muscovite-$2M_1$, and K-feldspar prevail, with small amounts of dolomite, kaolinite, chlorite, barite, jarosite, dawsonite, goethite, halite and Ti-oxides (Table 1; Fig. 6). The finer fractions (0.4–2, 0.1–0.4 µm) are enriched in mixed layer illite-smectite while inherited minerals gradually decrease progressively toward the <0.1 µm fraction, which only contains muscovite-$2M_1$ and mixed layer illite-smectite.

MY2305, MY2306, and MY2307 (Table 1; Fig. 6) are mainly composed of quartz (9–66 wt. %, for samples MY2306 and MY2305, respectively), muscovite-$2M_1$ (12–30 wt. %, for samples MY2305 and MY2307, respectively), K-feldspar (21–30 wt. %, for samples MY2305 and MY2306, respectively), and small amount of barite, jarosite, goethite, and Ti-oxides in the 6–10 µm and 2–6 µm grain-size fractions, that progressively disappear in the <0.1 µm fractions, which consist of

Table 1

Results of the Profex Rietveld refinement quantification of gouge samples EV39 and MY23/05/06/07/09/10/11. Minerals abbreviation: I-S: mixed layers illite-smectite (1M_d polytype): muscovite (2M_1 polytype), Kln: kaolinite, Chl: chlorite, Qz: quartz, Ant: anatase, Rt: rutile, Kfs: K-feldspar, Dol: dolomite, Gth: goethite, Mlc: malachite, Brt: barite, Jrs: jarosite, Dwn: dawsonite, Hl: halite; tr: traces (<1 %).

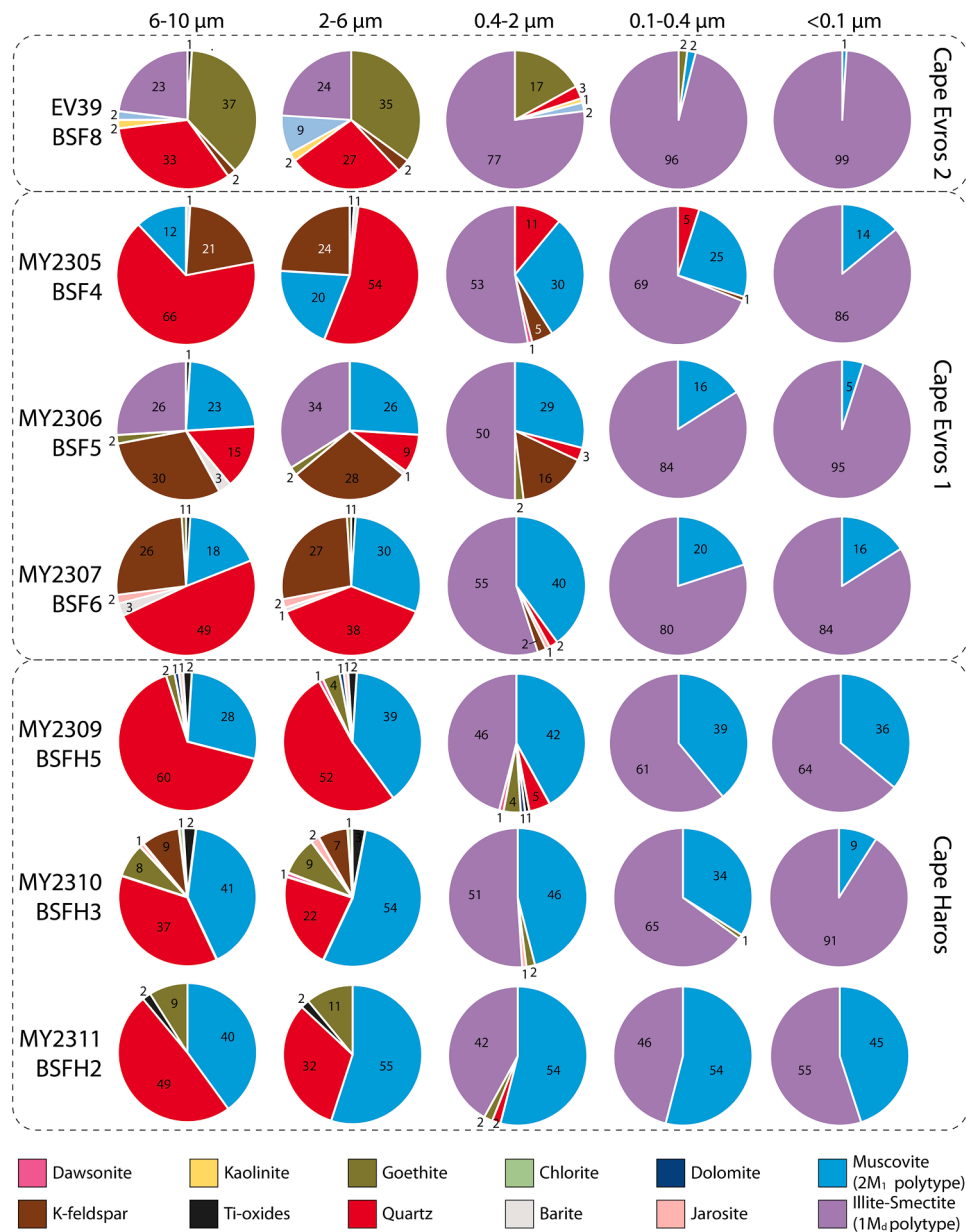| Sample ID | Size Fraction | BSF | whole-rock composition (wt.%) | | | | | | | | | | | | | | | Illite polytype normalised to 100% | |
| | | | I-S $1M_d$ | Ms $2M_1$ | Kln | Chl | Qz | Ant | Rt | Kfs | Dol | Gth | Mlc | Brt | Jrs | Dwn | Hl | I-S $1M_d$ | Ms $2M_1$ |
	(µm)																		
EV39	<0.1	8	99	1	-	-	-	-	-	-	-	-	-	-	-	-	-	99	1
	0.1-0.4		96	2	-	-	-	-	-	-	-	2	-	-	-	-	-	98	2
	0.4-2		77	2	1	-	3	-	-	-	-	17	-	-	-	-	-	97	3
	2-6		24	9	2	-	27	-	-	3	-	35	-	-	-	-	-	73	27
	6-10		23	2	2	-	33	1	-	2	-	37	-	-	-	-	-	92	8
MY2305	<0.1	4	86	14	-	-	-	-	-	-	-	-	-	-	-	-	-	86	14
	0.1-0.4		69	25	-	-	5	tr	-	1	-	-	-	-	-	tr	-	73	27
	0.4-2		53	30	-	-	11	tr	-	5	-	-	-	-	-	1	-	64	36
	2-6		0	20	-	-	54	1	-	24	-	-	tr	1	-	tr	-	0	100
	6-10		0	12	-	-	66	tr	-	21	-	-	tr	1	-	-	-	0	100
MY2306	<0.1	5	95	5	-	-	-	-	-	-	-	-	-	-	-	-	-	95	5
	0.1-0.4		84	16	-	-	-	-	-	-	-	-	-	-	-	-	-	84	16
	0.4-2		50	29	-	-	3	-	-	16	-	2	-	-	tr	-	-	63	37
	2-6		34	26	-	-	9	tr	-	28	-	2	-	1	tr	-	-	57	43
	6-10		26	23	-	-	15	1	-	30	-	2	-	3	tr	-	-	53	47
MY2307	<0.1	6	84	16	-	-	-	-	-	-	-	-	-	-	-	-	-	84	16
	0.1-0.4		80	20	-	-	-	-	-	-	-	-	-	-	-	-	-	80	20
	0.4-2		55	40	-	-	2	tr	-	2	-	-	-	1	-	-	-	58	42
	2-6		0	30	-	-	38	1	-	27	-	1	-	1	2	-	-	0	100
	6-10		0	18	-	-	49	1	-	26	-	1	-	3	2	-	-	0	100
MY2309	<0.1	H5	64	36	-	-	-	-	-	-	-	-	-	-	-	-	-	64	36
	0.1-0.4		61	39	-	-	-	-	-	-	-	-	-	-	-	-	-	61	39
	0.4-2		46	42	-	-	5	tr	1	-	1	4	-	-	-	1	-	52	48
	2-6		0	39	-	-	52	1	1	-	1	4	-	-	1	1	tr	0	100
	6-10		0	28	-	-	66	1	1	-	1	2	-	-	1	tr	tr	0	100
MY2310	<0.1	H3	79	21	-	-	-	-	-	-	-	-	-	-	-	-	-	79	21
	0.1-0.4		65	34	-	-	-	-	-	-	-	1	-	-	-	-	-	66	34
	0.4-2		51	46	-	-	-	-	tr	-	-	2	-	-	1	-	-	53	47
	2-6		0	54	-	1	23	2	1	7	tr	9	-	-	2	1	tr	0	100
	6-10		0	41	-	1	37	2	1	9	tr	8	-	-	1	tr	tr	0	100
MY2311	<0.1	H2	55	45	-	-	-	-	-	-	-	-	-	-	-	-	-	55	45
	0.1-0.4		46	54	-	-	-	-	-	-	-	tr	-	-	-	-	-	46	54
	0.4-2		42	54	-	-	2	-	tr	-	-	2	-	-	-	-	-	44	56
	2-6		0	55	-	-	32	tr	2	-	-	11	-	-	-	-	-	0	100
	6-10		0	40	-	-	49	tr	2	-	-	9	-	-	-	-	-	0	100

Fig. 6. Whole-rock composition of grain size fraction separated from gouge samples.

mixed layer illite-smectite (69–95 wt. %, for samples MY2305 and MY2306, respectively) and muscovite-2M$_1$ (5–25 wt. %, for samples MY2306 and MY2305, respectively). Only sample MY2306 shows mixed layer illite-smectite in the coarser fractions (26–34 wt. %; Table 1; Fig. 6). EV39 shows a mineral assemblage composed of quartz, goethite, muscovite-2M$_1$, mixed layer illite-smectite, and minor K-feldspar and kaolinite in the 6–10 μm fraction. These minerals become progressively less abundant in the finer fractions, where a significant increase of mixed layer illite-smectite is instead observed from 23 wt. % to 99 wt. % (Table 1; Fig. 6).

MY2309, MY2310, and MY2311 are mainly composed of quartz (22–60 wt. %, for samples MY2310 and MY2309, respectively), muscovite-2M$_1$ (28–55 wt. %, for samples MY2309 and MY2311, respectively), goethite (2–11 wt. %, for samples MY2309 and MY2311, respectively), K-feldspar (7–9 wt. %, only in MY2310), and small amounts of dolomite, jarosite, dawsonite, and Ti-oxides in the coarser fractions (Table 1; Fig. 6). The neoformed mixed layer illite-smectite occurs from the 0.4–2 μm fractions and increases its content to 55–91 wt. % (for samples MY2311 and MY2310, respectively) in the finest

ones, together with 9–45 wt. % of muscovite-2M$_1$, (for samples MY2310 and MY2311, respectively).

4.2.1. Significance of the detected mineralogical assemblages

Detrital silicate minerals, quartz and K-feldspar in gouge samples likely derive from the hanging wall Miocene siliciclastic deposits, which contain granite and low-grade metamorphic rock clasts (e.g., Sànchez-Goméz et al., 2002). The gouge composition is fairly constant among the analysed BSFs suggesting that the detachment evolved at similar crustal levels during the multiple slip events registered by the different K-Ar gouge ages (see section below), and indicating that the Miocene siliciclastic deposits always formed the hanging wall of the MD during the studied deformation history. Additionally, the lack of high-grade metamorphic mineral phases within the gouge samples is indicative of the absence of blueschist and eclogite HP rocks within the basal portion of the siliciclastic deposits in the hanging wall (e.g., Sànchez-Goméz et al., 2002). Hydrothermal-related mineralogical phases (e.g., barite and Fe-Ti-oxides) crystallized from Fe- and Ba- rich fluids circulating within the fault zone during the progressive cooling of the

footwall granite during extension (e.g., Menant et al., 2013). Those phases occur in most of the grain size fractions (6–10, 2–6, 0.4–2, 0.1–0.4 μm) from all gouges and, at the outcrop, they are formed by (i) nodular concretions within gouge layers that cut across the foliation of the gouges (Fig. S4), commonly in association with a clear alteration halo (Fig. S4A), or (ii) veins at high angle to the foliation in the gouges (e.g., Menant et al., 2013) that cut across and the entire MD fault core. The latter observation suggests that the ingress of most hydrothermal fluids postdates gouge formation and the main fault activity. Occurrence of carbonate (e.g., dolomite, dawsonite, malachite) and sulphate minerals (e.g., jarosite), as well as halite, attest to the interaction of hydrothermal fluids with meteoric/marine waters due to the subaerial exposure and/or supergene conditions (e.g., Chukhrov, 1981; Fulignati, 2020; Marchesini et al., 2024).

4.3. K-Ar dating

K-Ar results are plotted in S6A and charted in Table 2. The results of the Illite Age Analysis (IAA – see below) are shown in Fig. 7A and S6B, where polytype proportions were normalized to 100 % (Fig. S5), and plotted as apparent K-Ar date versus percent of detrital illite, and linearly extrapolated to 0 % and 100 % illite/muscovite-2M$_1$ by York regression. Samples from CH, record a first slip event at 13.34 ± 0.77 Ma and 12.47 ± 0.40 Ma (BSFH3-H5, respectively; Serravallian, coeval with granite crystallisation; Figs. 7A-B, Table 2), recorded by mixed layer illite-smectite in gouges along C planes within the SC/C' domains of the fault zone, in the northwestern and more internal investigated exposure (Fig. 7B). Samples from CE1 and CE2 constrain four distinct slip events within a ~3 Myrs time span (Fig. 7A-B, Table 2). The first slip recorded is at 9.75 ± 0.4 Ma (middle Tortonian, sample MY2305, BSF4; Fig. 7; Table 2). Considering that at Cape Haros (more internal and up-dip part of the detachment; Fig. 7B) there are no evidence of slip recorded by

Table 2
Summary of sampled and dated gouges from Cape Evros 1, 2 and Cape Haros exposures. IAA: K-Ar illite age analysis.

| Sample ID and BSF	Location	Grain-size fraction (μm)	^{40}Ar* Mass mg	mol/g	σ (%)	^{40}Ar* %	K Mass mg	wt %	σ (%)	K-Ar Age Data Age (Ma)	σ (Ma)	IAA K-Ar Age data Age (Ma)	σ (Ma)
EV39 BSF8	Cape Evros 2 37°28′26.47″N 25°27′31.04″E	<0.1	2.538	8.404E-11	1.07	50.6	50.7	6.780	1.35	7.1	±0.1	7.1	±0.17
		0.1-0.4	2.298	8.825E-11	1.12	52.4	52.0	7.053	1.31	7.2	±0.1		
		0.4-2	1.114	7.599E-11	2.31	51.5	51.0	6.172	1.40	7.1	±0.2		
		2-6	2.152	4.638E-11	1.95	42.0	50.5	3.362	1.65	7.9	±0.2		
		6-10	2.336	3.711E-11	2.24	34.8	50.6	2.873	1.70	7.4	±0.2		
MY2305 BSF4	Cape Evros 1 37°28′26.95″N 25°27′25.38″E	<0.1	2.310	1.22E-10	0.81	32.9	53.1	7.012	1.28	10.0	±0.2	9.5	±0.4
		0.1-0.4	2.128	1.754E-10	0.68	68.9	52.2	7.240	1.27	13.9	±0.2		
		0.4-2	4.164	2.854E-10	0.40	80.8	52.4	6.991	1.30	23.4	±0.3		
		2-6	3.818	2.24E-10	0.43	85.7	57.2	4.563	1.51	28.1	±0.4		
		6-10	2.186	1.370E-10	0.79	78.8	52.9	3.505	1.66	22.4	±0.4		
MY2306 BSF5	Cape Evros 1 37°28′26.95″N 25°27′25.38″E	<0.1	4.696	6.272E-11	0.78	46.2	50.3	4.006	1.63	9.0	±0.2	6.37	±0.21
		0.1-0.4	2.410	1.162E-10	0.80	37.6	51.3	5.863	1.43	11.4	±0.2		
		0.4-2	2.480	2.486E-10	0.50	67.0	51.7	6.590	1.35	21.6	±0.3		
		2-6	1.964	3.07E-10	0.52	77.7	50.9	6.959	1.32	25.2	±0.4		
		6-10	1.992	2.87E-10	0.53	74.7	50.9	6.786	1.34	24.2	±0.3		
MY2307 BSF6	Cape Evros 1 37°28′26.95″N 25°27′25.38″E	<0.1	1.116	1.49E-10	1.33	54.0	51.5	6.837	1.33	12.5	±0.2	8.07	±0.52
		0.1-0.4	1.440	1.95E-10	0.87	58.6	50.5	7.292	1.29	15.4	±0.2		
		0.4-2	3.240	2.93E-10	0.42	74.7	52.7	7.312	1.26	23.0	±0.3		
		2-6	1.866	4.31E-10	0.48	82.5	53.0	5.717	1.42	43.0	±0.6		
		6-10	3.096	3.13E-10	0.42	79.4	53.6	4.453	1.55	40.0	±0.6		
MY2309 BSFH5	Cape Haros 37°29′2.35″N 25°25′24.38″E	<0.1	3.522	3.4E-10	0.40	77.4	52.8	6.783	1.31	28.7	±0.4	13.34	±0.77
		0.1-0.4	1.584	5.260E-10	0.49	79.3	50.4	6.985	1.33	42.9	±0.6		
		0.4-2	3.312	7.38E-10	0.38	90.1	51.0	6.582	1.36	63.5	±0.9		
		2-6	2.868	4.47E-10	0.40	90.6	53.1	3.478	1.66	72.6	±1.2		
		6-10	2.326	3.004E-10	0.48	77.1	49.9	2.620	1.77	64.9	±1.2		
MY2310 BSFH3	Cape Haros 37°29′2.35″N 25°25′24.38″E	<0.1	3.778	2.909E-10	0.41	81.6	51.7	7.228	1.28	23.1	±0.3	12.47	±0.4
		0.1-0.4	3.636	4.58E-10	0.39	88.9	54.8	7.565	1.20	34.5	±0.4		
		0.4-2	2.858	7.32E-10	0.39	91.3	53.7	7.288	1.25	57.0	±0.7		
		2-6	2.432	1.09E-09	0.39	94.5	51.8	5.585	1.45	109.3	±1.6		
		6-10	3.426	8.81E-10	0.37	90.8	52.9	4.744	1.53	104.1	±1.6		
MY2311 BSFH2	Cape Haros 37°29′2.35″N 25°25′24.38″E	<0.1	3.822	3.29E-10	0.40	86.9	58.0	7.601	1.14	24.8	±0.3	-	-
		0.1-0.4	3.432	5.37E-10	0.38	90.6	52.2	7.760	1.22	39.5	±0.5		
		0.4-2	2.796	8.891E-10	0.39	93.7	51.5	7.353	1.27	68.4	±0.9		
		2-6	2.458	1.11E-09	0.39	94.3	50.7	4.692	1.56	131.8	±2.0		
		6-10	3.130	9.28E-10	0.38	92.5	50.6	3.693	1.66	139.3	±2.3		
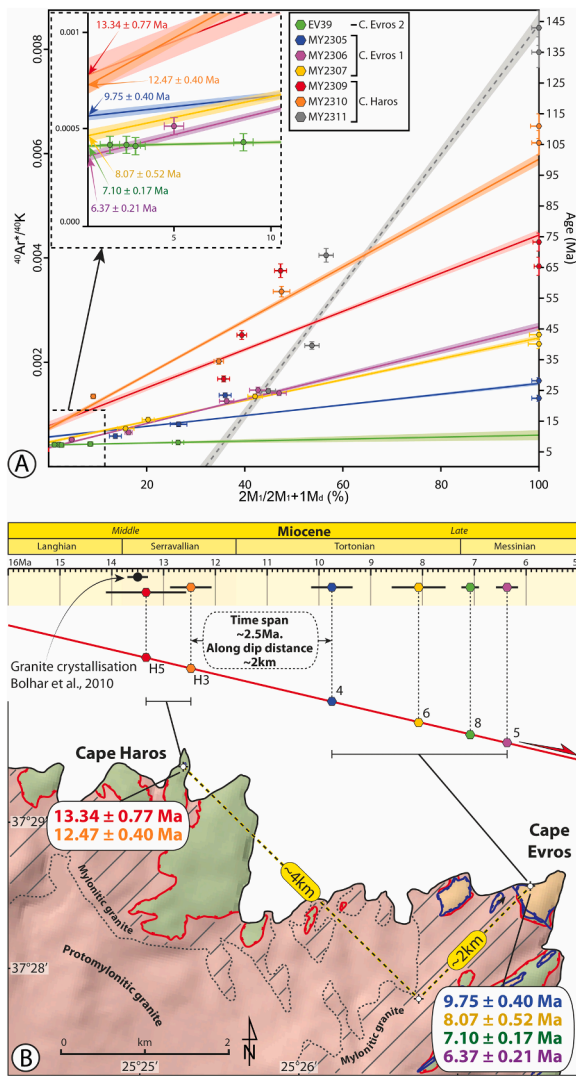
Fig. 7. (A) Illite Age Analysis by using York regression. (B) Spatial and temporal dispersion of IAA ages. The position of ages in the two outcrops is shown in panel B. See Fig. 1 for the rock unit and structural elements legend.

gouge formation younger than ~12.5 Ma (Fig. 8A-B), the 9.75 ± 0.4 Ma age constrains the down-dip migration of deformation localisation from Cape Haros to Cape Evros sector, which forms the more external and down-dip exposed part of the detachment (Figs. 7B and 8). The other three gouges from CE1 and CE2 constrain protracted faulting at 8.07 ± 0.52 Ma, 6.37 ± 0.21 Ma (samples MY2307 – BSF6 and MY2306 - BSF5, respectively; Fig. 7; Table 2) and 7.10 ± 0.17 Ma (sample EV39 – BSF8; Fig. 7; Table 2), thus documenting deformation localisation from the middle-upper Tortonian to the middle Messinian (Fig. 7B). These ages thus record ~2 km of down-dip migration of deformation localisation during a ~2.5 Myrs time interval (Fig. 7B), which constrains an average ~1mm/yr slip rate during the formation of the detachment (Fig. 7B). BSFH2 did not yield a meaningful age, with a negative intercept at 0 % illite/muscovite-2M$_1$ (Fig. 3C) due to the large amount of detrital illite/muscovite in the finer fractions (Figs. 4 and 5; Table 1).

5. Discussion and conclusions

In comparison to other brittle detachments representing the relatively late evolution stage of early and successively deactivated ductile shear zones (e.g., Tinos Detachment, Simplon Detachment; Mehl et al., 2005; Montemagni and Zanchetta, 2022), the MD is a remarkable

example of an extensional detachment nucleating and evolving entirely under brittle conditions. The MD thus provides useful insights into how deformation in the upper brittle crust progressively localises during crustal-scale rifting, footwall exhumation and synkinematic magmatism (Fig. 8). Starting from our data, we present a conceptual and time-constrained model (Fig. 8) for the evolution of such rifting-related crustal-scale structures. From base to top, the tectonic stack in the model (Fig. 8), is composed of:

- The Cycladic basement, in the middle-lower crust, representing part of the footwall of the ductile basal detachment (e.g., Jolivet et al., 2010);
- The Cycladic Blueschist unit in the footwall of the ductile basal detachment, (e.g., Jolivet et al., 2010);
- A syntectonic granite pluton, which emplaced, was exhumed and cooled down in response to strain localising along the Livada ductile basal detachment at mid- to deep-crustal conditions;
- An upper plate, representing (i) the hanging wall of the Livada ductile basal detachment and (ii) the footwall of the MD brittle detachment in the upper crust;
- Syntectonic siliciclastic deposits representing the structurally higher unit and infilling a range of supradetachment basins, in the hanging wall of the MD brittle detachment.

We propose that, while ductile fabrics formed at lower to middle crustal conditions allowing for granite emplacement and progressive exhumation (~15 Ma; Fig. 8A), detachment hinge-rolling and progressive crustal thinning were accommodated by multiple, moderately dipping brittle detachments (such as the MD) that localised at shallow depth by forming incipient fault zones (Fig. 8A). Early brittle deformation localised therein at the boundary between the upper plate and syntectonic siliciclastic deposits, infilling supradetachment basins (Fig. 8A).

At ~13.5Ma, MD deformation localised at shallow structural levels with gouges along C surfaces (BSFsH3–5; site I; Fig. 8B), whereas deeper down deformation partitioned into SC domains (site II; Fig. 8B) reworking the upper plate and siliciclastic deposits, causing the overall widening of the MD (Fig. 8B). At the same time, the exhuming granite was progressively involved into the deformation along the Livada basal ductile detachment, and a ductile proto-mylonitic shear zone started to form at the top of the uprising pluton (Fig. 8B). After 2.5 Myrs, basin deepening and increasing extension caused the MD deformation to migrate down-dip (from site I to site II in Fig. 8C) and the shallowest MD deactivated. As suggested by the absence of ages younger than ~12.5 Ma at site II (see paragraph 4.3 K-Ar DATING; Fig. 7) slip did no longer localise at that structural position, such that this part of the detachment can be thus considered as a "fossil" domain which underwent a progressive exhumation, recording and preserving the earliest deformation increments (as documented by our dating results; Fig. 8C). Down-dip deformation started to localise along the fault plane (site II, Fig. 8C) assisted by cataclasis and gouge formation (BSF4, 9.75 Ma; Fig. 8C), accompanied by further granite exhumation to shallow depths. This led to the progressive cooling of the granite, and to progressive deformation being accommodated within the ductile-brittle transition zone, even though ductile deformation continued to localise at deeper structural levels, on top of the granite, producing ultra-mylonitic fabrics (Fig. 8A-C).

The MD fault core (site II; Fig. 8D) grew farther down-dip, through progressive and continuous gouge formation, leading to fault narrowing through repeated slip (BSFs4, 5, 6, 8; 8.07 – 6.37 Ma; Fig. 8D). The end of granite exhumation (at ~8 Ma, (U-Th)/He apatite; Brichau et al. 2008) and cooling of the system triggered final deformation localisation at 6.37 Ma (BSF4; Fig. 8D), that is, ~7 Ma after faulting initiation (BSFH5, 13.34 Ma; Fig. 8A). Finally, a principal slip surface (PSS; <6.37 Ma; Fig. 8D) cut across all other domains, dissecting the fault core. High-angle secondary normal faults rooted into the PSS and cut across
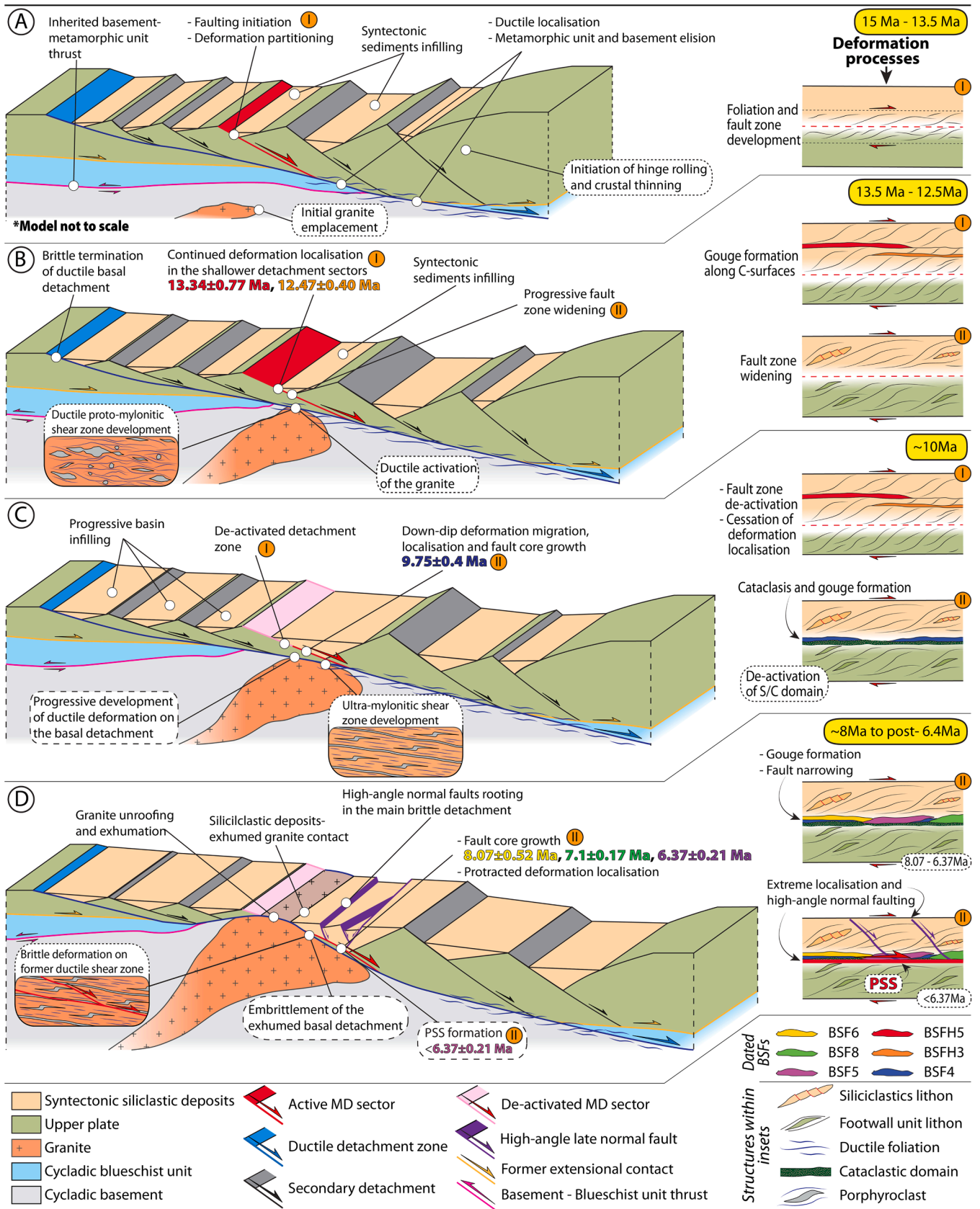
Fig. 8. Time-constrained model for brittle detachments evolution. (A) crustal thinning, hinge rolling and brittle-ductile detachment zones initiation. (B) Deformation localisation along the main brittle detachment, gouge formation and development of SC structure-dominated shear zone, coeval with the onset of ductile deformation along the upper part of the exhuming granite. (C) Down-dip deformation migration by cataclasis and gouge formation in the deep part of the brittle detachment coevally with the development of ultramylonites along the basal ductile detachment. (D) Protracted deformation and extreme localisation during the final stages of the granite exhumation. Late brittle overprint on the early ductile fault architecture after the complete exhumation of the granite.

the siliciclastic deposits (that in the meantime had infilled the supra-detachment basins and became juxtaposed against the exhumed granite; Fig. 8D), while brittle structures progressively overprinted former ductile fabrics along the top of the already deformed granite in the footwall (Fig. 8D).

This model depicts the evolution of a dynamic detachment system at shallow crustal levels during the uplift, cooling and exhumation of a granite pluton, in which the first crystallisation of the granite is coeval with the onset of brittle deformation in the upper crust (Fig. 8). Our study makes it possible to completely constrain the activation of various deformation mechanisms through space and time and to define their role in forming brittle shallow detachments that shape upper crustal architectures (Fig. 8). New high-precision geochronological constraints covering a ~7 Ma time interval (Fig. 7) document coeval brittle and ductile deformation, steering regional crustal thinning and footwall exhumation through protracted deformation (Figs. 7 and 8). Early localisation (~15–13.5 Ma, from the granite crystallisation to first gouge formation, respectively; Figs. 7 and 8) attests to a rapid shear zone structuring, where the hanging wall siliciclastics, infilling basins, are rapidly involved in SC/C' domain formation (Fig. 8).

For the first time, we could constrain a complete suite of structures along a brittle detachment that never exploited former ductile fabrics during its evolution, and document the evolution through-time of the progressive deformation mechanisms migration under brittle conditions along the detachment (Figs. 7 and 8). Deformation localisation took (i) ~2.5 Ma to migrate dip-ward, as testified by first cataclasis in Fig. 8C and (ii) further ~3.4 Ma to reach conditions triggering a slip plane formation, which can localise and propagate only after granite exhumation and system cooling, also corresponding to the embrittlement of the exhumed ductile basal detachment that at that stage put in contact the siliciclastic deposits directly onto the granite (Fig. 8D). Our new ages, constraining 6 slip events through at least 7 Myrs-long protracted deformation localisation along the same detachment, point the attention on the importance of fault architecture analysis, sampling and dating of its structural domains. Even though detailed constraints on the absolute dating of brittle detachments do exist (e.g., Haines and van der Pluijm, 2008; Hetzel et al., 2013; Mancktelow et al., 2016; Heineke et al., 2019; Münch et al., 2021), in most cases they only constrain one single age of activation of the investigated structure or, alternatively, do not take into account the relationship between ages and deformation mechanisms along the detachments, running the risk of oversimplifying fault evolution histories. Our data prove instead that complex and mature faults and detachments, such as the MD, are intricated objects, made of a plethora of tectonic structures activated at different times during a long deformation history. Our approach (e.g., sampling, analysis and dating of every fault gouge) demonstrates that even in a short time span (~7 Myrs in our study) a single age cannot describe the entire fault evolution, which is instead documented by several ages recording multiple and protracted slip along the same structure. These findings might have a strong impact also on the consideration of such structures from a regional perspective, being their activation central also toward the understanding of deformation partitioning in both the lower and upper crust during the exhumation of even deeply subducted crustal slices. We thus demonstrate that only a detailed analysis as that applied can deconvolute such complex histories.

In conclusion, this study documents the overall response of the upper brittle crust during the onset and evolution of crustal-scale stretching as accommodated at shallow depth by brittle low-angle detachments. We provide for the first time a time-constrained model that efficiently accounts for how, when, and in what time span brittle detachments can form, and how deformation localises or partition in response to crustal thinning, footwall exhumation and synkinematic magmatism. Our results provide novel insights that are readily applicable to similar detachments elsewhere, in the context of rift and metamorphic core complex systems.

CRediT authorship contribution statement

C. Zuccari: Writing – review & editing, Writing – original draft, Visualization, Methodology, Investigation, Formal analysis, Data curation, Conceptualization. **F. Mazzarini:** Writing – review & editing, Visualization, Supervision, Methodology, Investigation. **E. Tavarnelli:** Writing – review & editing, Validation, Supervision, Methodology, Investigation. **G. Viola:** Writing – review & editing, Project administration, Funding acquisition. **L. Aldega:** Writing – review & editing, Visualization, Validation, Formal analysis, Data curation. **V. Moretto:** Writing – review & editing, Visualization, Validation, Formal analysis, Data curation. **R. Xie:** Validation, Formal analysis. **G. Musumeci:** Writing – review & editing, Supervision, Project administration, Methodology, Investigation, Data curation.

Declaration of competing interest

The authors declare the following financial interests/personal relationships which may be considered as potential competing interests: Giulio Viola reports financial support was provided by Italian Ministry for University and Research (MUR). If there are other authors, they declare that they have no known competing financial interests or personal relationships that could have appeared to influence the work reported in this paper.

Acknowledgements

Supplementary materials

Supplementary material associated with this article can be found, in the online version, at doi:10.1016/j.epsl.2024.119108.

Data availability

Data will be made available on request.

References

Aldega, L., Viola, G., Casas-Sainz, A., Marcén, M., Román-Berdiel, T., van der Lelij, R., 2019. Unraveling multiple thermotectonic events accommodated by crustal-scale faults in Northern Iberia, Spain: insights from K-Ar dating of clay gouges. Tectonics 38, 3629–3651. https://doi.org/10.1029/2019TC005585.

Aravadinou, E., Gerogiannis, N., Xypolias, P., 2022. Development and passive exhumation of high-pressure shear zones (Blueschist Unit, Syros): insights from quartz and columnar calcite microstructures. J. Struct. Geol. 159, 104607. https://doi.org/10.1016/j.jsg.2022.104607.

Bakowsky, C., Schneider, D.A., Grasemann, B., Soukis, K., 2023. Miocene ductile thinning below the folegandros detachment system, Cyclades, Greece. Terra Nova. https://doi.org/10.1111/ter.12646.

Bolhar, R., Ring, U., Allen, C.M., 2010. An integrated zircon geochronological and geochemical investigation into the Miocene plutonic evolution of the Cyclades, Aegean Sea, Greece: part 1: geochronology. Contrib. Mineral. Petrol. 160, 719–742. https://doi.org/10.1007/s00410-010-0504-4.

Braathen, A., Tveranger, J., Fossen, H., Skar, T., Cardozo, N., Semshaug, S.E., Bastesen, E., Sverdrup, E., 2009. Fault facies and its application to sandstone reservoirs. Am. Assoc. Pet. Geol. Bull. 93, 891–917. https://doi.org/10.1306/03230908116.

Brichau, S., Ring, U., Carter, A., Bolhar, R., Monié, P., Stockli, D., Brunel, M., 2008. Timing, slip rate, displacement and cooling history of the Mykonos detachment footwall, Cyclades, Greece, and implications for the opening of the Aegean Sea basin. J. Geol. Soc. London 165, 263–277. https://doi.org/10.1144/0016-76492006-145.

Brichau, S., Ring, U., Ketcham, R.A., Carter, A., Stockli, D., Brunel, M., 2006. Constraining the long-term evolution of the slip rate for a major extensional fault

system in the central Aegean, Greece, using thermochronology. Earth Planet. Sci. Lett. 241, 293–306. https://doi.org/10.1016/j.epsl.2005.09.065.

Brichau, S., Thomson, S., Ring, U., 2010. Thermochronometric constraints on the tectonic evolution of the serifos detachment, Aegean Sea, Greece. Int. J. Earth Sci. 99, 379–393. https://doi.org/10.1007/s00531-008-0386-0.

Chukhrov, F.V., 1981. Convergence of certain supergene and hypogene processes of mineral formation. Int. Geol. Rev. 23, 1401–1411. https://doi.org/10.1080/00206818209467277.

Coleman, M., Dubosq, R., Schneider, D.A., Grasemann, B., Soukis, K., 2019. Along-strike consistency of an extensional detachment system, West Cyclades, Greece. Terra Nova 31, 220–233. https://doi.org/10.1111/TER.12388.

Cottle, J.M., Jessup, M.J., Newell, D.L., Searle, M.P., Law, R.D., Horstwood, M.S.A., 2007. Structural insights into the early stages of exhumation along an orogen-scale detachment: the South Tibetan Detachment System, Dzakaa Chu section, Eastern Himalaya. J. Struct. Geol. 29, 1781–1797. https://doi.org/10.1016/j.jsg.2007.08.007.

Curzi, M., Viola, G., Zuccari, C., Aldega, L., Billi, A., van der Lelij, R., Kylander-Clark, A., Vignaroli, G., 2024. Tectonic Evolution of the Eastern Southern Alps (Italy): a reappraisal from new structural data and geochronological constraints. Tectonics 43, e2023TC008013. https://doi.org/10.1029/2023TC008013.

Dinter, D.A., Royden, L., 1993. Late Cenozoic extension in northeastern Greece: strymon Valley detachment system and Rhodope metamorphic core complex. Geology 21, 45–48.

Faure, M., Bonneau, M., Pons, J., 1991. Ductile deformation and syntectonic granite emplacement during the late Miocene extension of the Aegea (Greece). Bulletin de la Société Géologique de France 162, 3–11. https://doi.org/10.2113/gssgfbull.162.1.3.

Fossen, H., Cavalcante, G.C.G., 2017. Shear zones – A review. Earth Sci. Rev. 171, 434–455. https://doi.org/10.1016/J.EARSCIREV.2017.05.002.

Fulignati, P., 2020. Clay minerals in hydrothermal systems. Minerals 10, 919. https://doi.org/10.3390/min10100919.

Gautier, P., Brun, J-P, Jolivet, L., 1993. Structure and kinematics of upper cenozoic extensional detachment on naxos and paros (Cyclades Islands, Greece). Tectonics 12, 1180–1194. https://doi.org/10.1029/93TC01131.

Gazzola, R., Zuccari, C., Frassi, C., Xypolias, P., Musumeci, G., 2023. Structural setting and architecture of the north cycladic detachment system in the northeastern sectors of Mykonos Island (Greece). J Maps 19. https://doi.org/10.1080/17445647.2023.2277387.

Glodny, J., Ring, U., 2022. The Cycladic Blueschist Unit of the Hellenic subduction orogen: protracted high-pressure metamorphism, decompression and reimbrication of a diachronous nappe stack. Earth Sci. Rev. 224. https://doi.org/10.1016/J.EARSCIREV.2021.103883.

Grasemann, B., Huet, B., Schneider, D.A., Rice, A.H.N., Lemonnier, N., Tschegg, C., 2018. Miocene postorogenic extension of the Eocene synorogenic imbricated Hellenic subduction channel: new constraints from Milos (Cyclades, Greece). GSA Bull. 130, 238–262. https://doi.org/10.1130/B31731.1.

Grasemann, B., Schneider, D.A., Stöckli, D.F., Iglseder, C., 2012. Miocene bivergent crustal extension in the Aegean: evidence from the western Cyclades (Greece). Lithosphere 4, 23–39. https://doi.org/10.1130/L164.1.

Grosjean, G., Sue, C., Burkhard, M., 2004. Late Neogene extension in the vicinity of the Simplon fault zone (central Alps, Switzerland). Eclogae Geol. Helv. 97, 33–46. https://doi.org/10.1007/s00015-004-1114-9.

Haines, S.H., van der Pluijm, B.A., 2012. Patterns of mineral transformations in clay gouge, with examples from low-angle normal fault rocks in the western USA. J. Struct. Geol. 43, 2–32. https://doi.org/10.1016/J.JSG.2012.05.004.

Haines, S.H., van der Pluijm, B.A., 2008. Clay quantification and Ar–Ar dating of synthetic and natural gouge: application to the Miocene Sierra Mazatán detachment fault. J. Struct. Geol. 30, 525–538. https://doi.org/10.1016/j.jsg.2007.11.012.

Hartz, E.H., Andresen, A., Martin, M.W., Hodges, K.V., 2000. U–Pb and ^{40}Ar/^{39}Ar constraints on the fjord region detachment zone: a long-lived extensional fault in the central East Greenland Caledonides. J. Geol. Soc. London 157, 795–809. https://doi.org/10.1144/jgs.157.4.795.

Heineke, C., Hetzel, R., Nilius, N.P., Zwingmann, H., Todd, A., Mulch, A., Wölfler, A., Glotzbach, C., Akal, C., Dunkl, I., Raven, M., Hampel, A., 2019. Detachment faulting in a bivergent core complex constrained by fault gouge dating and low-temperature thermochronology. J. Struct. Geol. 127, 103865. https://doi.org/10.1016/J.JSG.2019.103865.

Hejl, E., Riedl, H., Weingartner, H., 2002. Post-plutonic unroofing and morphogenesis of the Attic-Cycladic complex (Aegea, Greece). Tectonophysics 349, 37–56.

Hetzel, R., Zwingmann, H., Mulch, A., Gessner, K., Akal, C., Hampel, A., Güngör, T., Petschick, R., Mikes, T., Wedin, F., 2013. Spatiotemporal evolution of brittle normal faulting and fluid infiltration in detachment fault systems: a case study from the Menderes Massif, western Turkey. Tectonics 32, 364–376. https://doi.org/10.1002/tect.20031.

Isik, V., Tekeli, O., Seyitoglu, G., 2004. The 40Ar/39Ar age of extensional ductile deformation and granitoid intrusion in the northern Menderes core complex: implications for the initiation of extensional tectonics in western Turkey. J. Asian Earth Sci. 23, 555–566. https://doi.org/10.1016/J.JSEAES.2003.09.001.

Johnston, S.M., Hacker, B.R., Andersen, T.B., 2007. Exhuming Norwegian ultrahigh-pressure rocks: overprinting extensional structures and the role of the Nordfjord-Sogn Detachment Zone. Tectonics 26. https://doi.org/10.1029/2005TC001933.

Jolivet, L., Brun, J.P., 2010. Cenozoic geodynamic evolution of the Aegean. Int. J. Earth Sci. 99, 109–138. https://doi.org/10.1007/s00531-008-0366-4.

Jolivet, L., Faccenna, C., 2000. Mediterranean extension and the Africa-Eurasia collision. Tectonics 19, 1095–1106. https://doi.org/10.1029/2000TC900018.

Jolivet, L., Lecomte, E., Huet, B., Denèle, Y., Lacombe, O., Labrousse, L., Le Pourhiet, L., Mehl, C., 2010. The north cycladic detachment system. Earth Planet. Sci. Lett. 289, 87–104. https://doi.org/10.1016/j.epsl.2009.10.032.

Jolivet, L., Menant, A., Sternai, P., Rabillard, A., Arbaret, L., Augier, R., Laurent, V., Beaudoin, A., Grasemann, B., Huet, B., Labrousse, L., Le Pourhiet, L., 2015. The geological signature of a slab tear below the Aegean. Tectonophysics 659, 166–182. https://doi.org/10.1016/j.tecto.2015.08.004.

Jolivet, L., Sautter, V., Moretti, I., Vettor, T., Papadopoulou, Z., Augier, R., Denèle, Y., Arbaret, L., 2021. Anatomy and evolution of a migmatite-cored extensional metamorphic dome and interaction with syn-kinematic intrusions, the Mykonos-Delos-Rheneia MCC. J. Geodyn. 144, 101824. https://doi.org/10.1016/J.JOG.2021.101824.

La Roche, R.S., Godin, L., Cottle, J.M., Kellett, D.A., 2016. Direct shear fabric dating constrains early Oligocene onset of the South Tibetan detachment in the western Nepal Himalaya. Geology 44, 403–406. https://doi.org/10.1130/G37754.1.

Lecomte, E., Jolivet, L., Lacombe, O., Denèle, Y., Labrousse, L., Le Pourhiet, L., 2010. Geometry and kinematics of Mykonos detachment, Cyclades, Greece: evidence for slip at shallow dip. Tectonics 29. https://doi.org/10.1029/2009TC002564.

Lee, J., Lister, G.S., 1992. Late Miocene ductile extension and detachment faulting, Mykonos, Greece. Geology 20, 121–124.

Lister, G.S., Davis, G.A., 1989. The origin of metamorphic core complexes and detachment faults formed during Tertiary continental extension in the northern Colorado River region. U.S.A. J Struct Geol 11, 65–94. https://doi.org/10.1016/0191-8141(89)90036-9.

Mancktelow, N., Zwingmann, H., Mulch, A., 2016. Timing and conditions of clay fault gouge formation on the Naxos detachment (Cyclades, Greece). Tectonics 35, 2334–2344. https://doi.org/10.1002/2016TC004251.

Marchesini, B., Tavani, S., Mercuri, M., Mondillo, N., Pizzati, M., Balsamo, F., Aldega, L., Carminati, E., 2024. Structural control on the alteration and fluid flow in the lithocap of the Allumiere-Tolfa epithermal system. J. Struct. Geol. 179, 105035. https://doi.org/10.1016/j.jsg.2023.105035.

Mehl, C., Jolivet, L., Lacombe, O., 2005. From ductile to brittle: evolution and localization of deformation below a crustal detachment (Tinos, Cyclades, Greece). Tectonics 24, 1–23. https://doi.org/10.1029/2004TC001767.

Mehl, C., Jolivet, L., Lacombe, O., Labrousse, L., Rimmele, G., 2007. Structural evolution of andros (Cyclades, Greece): a key to the behaviour of a (flat) detachment within an extending continental crust. Geol. Soc. Spec. Publ. 291, 41–73. https://doi.org/10.1144/SP291.3.

Menant, A., Jolivet, L., Augier, R., Skarpelis, N., 2013. The north cycladic detachment system and associated mineralization, Mykonos, Greece: insights on the evolution of the Aegean domain. Tectonics 32, 433–452. https://doi.org/10.1002/tect.20037.

Montemagni, C., Zanchetta, S., 2022. Constraining kinematic and temporal evolution of a normal-sense shear zone: insights into the Simplon Shear Zone (Western Alps). J. Struct. Geol. 156, 104557. https://doi.org/10.1016/j.jsg.2022.104557.

Mulch, A., Cosca, M., Andresen, A., Fiebig, J., 2005. Time scales of deformation and exhumation in extensional detachment systems determined by high-spatial resolution in situ UV-laser 40Ar/39Ar dating. Earth Planet. Sci. Lett. 233, 375–390. https://doi.org/10.1016/j.epsl.2005.01.042.

Münch, P., Caillaud, J., Monié, P., Grauby, O., Corsini, M., Ricci, J., Romagny, A., Philippon, M., Lanson, B., Azdimousa, A., Ben Moussa, A., Arnaud, N., 2021. Direct dating of brittle extensional deformation contemporaneous of Neogene exhumation of the internal zones of the Rif Chain. Tectonophysics 807, 228800. https://doi.org/10.1016/j.tecto.2021.228800.

Musumeci, G., Mazzarini, F., Cruden, A.R., 2015. The zuccale fault, Elba Island, Italy: a new perspective from fault architecture. Tectonics 34, 1195–1218. https://doi.org/10.1002/2014TC003809.

Pevear, D.R., 1999. Illite and hydrocarbon exploration. Proc. Natl. Acad. Sci. 96, 3440–3446. https://doi.org/10.1073/pnas.96.7.3440.

Ring, U., Gessner, K., Güngör, T., Passchier, C.W., 1999. The menderes massif of western Turkey and the cycladic massif in the aegean-do they really correlate? J. Geol. Soc. London 156, 3–6. https://doi.org/10.1144/GSJGS.156.1.0003.

Ring, U., Glodny, J., Will, T.M., Thomson, S., 2011. Normal faulting on Sifnos and the South Cycladic Detachment System, Aegean Sea, Greece. J. Geol. Soc. London 168, 751–768. https://doi.org/10.1144/0016-76492010-064.

Rosenbaum, G., Avigad, D., Sánchez-Gómez, M., 2002. Coaxial flattening at deep levels of orogenic belts: evidence from blueschists and eclogites on Syros and Sifnos (Cyclades, Greece). J. Struct. Geol. 24, 1451–1462. https://doi.org/10.1016/S0191-8141(01)00143-2.

Rossetti, F., Asti, R., Faccenna, C., Gerdes, A., Lucci, F., Theye, T., 2017. Magmatism and crustal extension: constraining activation of the ductile shearing along the Gediz detachment, Menderes Massif (western Turkey). LithosLithos 282–283, 145–162. https://doi.org/10.1016/J.LITHOS.2017.03.003.

Sànchez-Gómez, M., Avigad, D., Heimann, A., 2002. Geochronology of clasts in allochthonous Miocene sedimentary sequences on Mykonos and Paros Islands: implications for back-arc extension in the Aegean Sea. J. Geol. Soc. London 159, 45–60.

Schneider, S., Hammerschmidt, K., Rosenberg, C.L., 2013. Dating the longevity of ductile shear zones: insight from 40Ar/39Ar in situ analyses. Earth Planet. Sci. Lett. 369–370, 43–58. https://doi.org/10.1016/j.epsl.2013.03.002.

Singleton, J.S., Stockli, D.F., Gans, P.B., Prior, M.G., 2014. Timing, rate, and magnitude of slip on the Buckskin-Rawhide detachment fault, west central Arizona. Tectonics 33, 1596–1615. https://doi.org/10.1002/2013TC003517.

Tartaglia, G., Ceccato, A., Scheiber, T., van der Lelij, R., Schönenberger, J., Viola, G., 2023. Time-constrained multiphase brittle tectonic evolution of the onshore mid-Norwegian passive margin. GSA Bull. 135, 621–642. https://doi.org/10.1130/B36312.1.

Tartaglia, G., Viola, G., van der Lelij, R., Scheiber, T., Ceccato, A., Schönenberger, J., 2020. Brittle structural facies" analysis: a diagnostic method to unravel and date multiple slip events of long-lived faults. Earth Planet. Sci. Lett. 545. https://doi.org/10.1016/j.epsl.2020.116420.

Torgersen, E., Viola, G., 2014. Structural and temporal evolution of a reactivated brittle-ductile fault - part I: fault architecture, strain localization mechanisms and deformation history. Earth Planet. Sci. Lett. 407, 205–220. https://doi.org/10.1016/j.epsl.2014.09.019.

Van Der Pluijm, B.A., Hall, C.M., Vrolijk, P.J., Pevear, D.R., Covey, M.C., 2001. The dating of shallow faults in the Earth's crust. Nature 412 (6843), 172–175. https://doi.org/10.1038/35084053, 2001412.

Vignaroli, G., Faccenna, C., Rossetti, F., 2009. Retrogressive fabric development during exhumation of the Voltri Massif (Ligurian Alps, Italy): arguments for an extensional origin and implications for the Alps-Apennines linkage. Int. J. Earth Sci. 98, 1077–1093. https://doi.org/10.1007/S00531-008-0305-4/FIGURES/11.

Viola, G., Musumeci, G., Mazzarini, F., Tavazzani, L., Curzi, M., Torgersen, E., van der Lelij, R., Aldega, L., 2022. Structural characterization and K–Ar illite dating of reactivated, complex and heterogeneous fault zones: lessons from the Zuccale Fault, Northern Apennines. Solid Earth 13, 1327–1351. https://doi.org/10.5194/se-13-1327-2022.

Viola, G., Scheiber, T., Fredin, O., Zwingmann, H., Margreth, A., Knies, J., 2016. Deconvoluting complex structural histories archived in brittle fault zones. Nat. Commun. 7 (1), 1–10. https://doi.org/10.1038/ncomms13448, 20167.

Viola, G., Torgersen, E., Mazzarini, F., Musumeci, G., van der Lelij, R., Schönenberger, J., Garofalo, P.S., 2018. New constraints on the evolution of the inner northern apennines by K-Ar dating of late miocene-early pliocene compression on the Island of Elba, Italy. Tectonics 37, 3229–3243. https://doi.org/10.1029/2018TC005182.

Wu, X., Zhu, G., Yin, H., Su, N., Lu, Y., Zhang, S., Xie, C., 2020. Origin of low-angle ductile/brittle detachments: examples from the cretaceous linglong metamorphic core complex in eastern China. Tectonics 39. https://doi.org/10.1029/2020TC006132.